Zhou et al. Nanoscale Research Letters (2016) 11:193
DOI 10.1186/s11671-016-1408-7

Nanoscale Research Letters

NANO EXPRESS Open Access

In Situ Fabrication of $Bi_2Ti_2O_7/TiO_2$ Heterostructure Submicron Fibers for Enhanced Photocatalytic Activity

Di Zhou[1*], Hu Yang[1], Yafang Tu[1], Yu Tian[1], Yaxuan Cai[2], Zhenglong Hu[3] and Xiaolong Zhu[1]

Abstract

A facile two-step synthesis route combining electrospinning and hydrothermal techniques has been performed to obtain $Bi_2Ti_2O_7/TiO_2$ heterostructured submicron fibers. $Bi_2Ti_2O_7$ nanosheets were grown on the surface of TiO_2 submicron fibers. The density of the nanosheets increased with higher precursor concentration of the Bi/Ti reaction raw materials. UV-visible (UV-vis) diffuse reflectance spectroscopy indicated that the absorption spectrum of the $Bi_2Ti_2O_7/TiO_2$ composite extended into the visible-light region. Photocatalytic tests showed that the $Bi_2Ti_2O_7/TiO_2$ heterostructures possess a much higher degradation rate of rhodamine B than the unmodified TiO_2 submicron fibers under visible light. The enhanced photocatalytic activity can be attributed to the synergistic effect between improved visible-light absorption and the internal electric field created by the heterojunctions. The effective separation of photogenerated carriers driven by the photoinduced potential was demonstrated by the photoelectrochemical analysis.

Keywords: Bismuth titanate, Heterostructure, Hydrothermal, Visible light, Photocatalyst

Background

Over the past decades, a large number of metal oxides have been explored for the purpose of photocatalytic degradation of harmful organic substances and hydrogen production through splitting water. Titanium dioxide (TiO_2) is widely regarded as a heterogeneous photocatalyst for the photodegradation of pollutants in wastewater due to its low-cost, strong oxidizing power, non-toxicity, and long-term photostability [1–4]. For certain practical applications, however, pure TiO_2 is not very suitable because it only absorbs UV light at wavelengths no longer than 387.5 nm (anatase phase) or 413.3 nm (rutile phase). Even complete absorption in that range would account for less than 5 % of incoming solar light energy. Additionally, the high recombination rate of photogenerated electron-hole pairs is another problem if TiO_2 is used for photocatalysis [4]. A common method used to overcome these drawbacks is to create a heterojunction composite comprising a TiO_2 bottom-layer and a different top-layer semiconductor with a narrow band gap. That way, the built-in potential gradient at the interface between the semiconductors facilitates the separation of electron-hole pairs and reduces the chance of recombination [5–8]. For effective sensitization of TiO_2 using another semiconductor to capture a larger part of the solar spectrum, the second semiconductor should meet the following conditions [5, 6]: (1) be a narrow band gap semiconductor; (2) possess a lower anodic conduction band (CB) than TiO_2; (3) possess high stability to prevent photocorrosion; and (4) be a visible light-driven photocatalyst itself. Thus, the development of suitable methods to fabricate narrow band gap semiconductor/TiO_2 heterojunction composites will be essential for the practical application of TiO_2 as photocatalyst.

Bismuth titanates, a large family that includes several phases of the Bi-O-Ti system, including $Bi_2Ti_4O_{11}$, $Bi_2Ti_2O_7$, $Bi_4Ti_3O_{12}$, $Bi_{20}TiO_{32}$, and $Bi_{12}TiO_{20}$, are promising candidates for many technological applications [9–14]. Several of these materials have been reported as visible light-driven photocatalysts, for example: $Bi_2Ti_2O_7$ nanorods, $Bi_{12}TiO_{20}$ nanowires, and $Bi_{20}TiO_{32}$ nanosheets [12–14]. Especially, $Bi_2Ti_2O_7$ with its

* Correspondence: zhdijhu@gmail.com
[1]School of Physics and Information Engineering, Jianghan University, Wuhan 430056, China
Full list of author information is available at the end of the article

pyrochlore structure forms a shallow acceptor energy level in the forbidden band because of a non-stoichiometric ratio of $Bi_{1.74}Ti_2O_{6.62}$ and the Bi vacancy [15]. As a result, the holes in $Bi_2Ti_2O_7$ can be excited into the valence band (VB) under irradiation with visible light. Bian and Ren et al. reported independently that $Bi_2Ti_2O_7$ absorbs well in the visible region and also possesses enhanced photocatalytic activity with regard to the decomposition of rhodamine B (RhB) under visible light [16, 17]. However, the fast recombination of photogenerated electron-hole pairs seriously limits energy-conversion efficiency. To promote the separation of photogenerated carriers in $Bi_2Ti_2O_7$, designing a composite photocatalyst by coupling $Bi_2Ti_2O_7$ with a semiconductor with matched band potentials is a sensible strategy. For example, Wang and Hou et al. reported independently that $Bi_2Ti_2O_7/TiO_2$ composite powders and nanowire arrays showed higher photocatalytic activity than pure TiO_2 under visible light [18–20]. Based on the above considerations, the authors constructed a novel $Bi_2Ti_2O_7$ sensitized TiO_2 composite system, with the goal to expand the photocatalytic activity of TiO_2 into the visible-light range. However, the photocatalytic performance of common composite films with a dense and smooth surface is still moderate. This is because the redox reaction occurs on the surface of catalyst film, and the surface morphology of the catalyst film plays a key role in the photocatalytic property [20–22]. Therefore, $Bi_2Ti_2O_7$ nanosheets-TiO_2 submicron fibers heterostructures were chosen as tested candidates and fabricated by using a combination of an electrospinning technique and hydrothermal method.

In this work, a facile in situ hydrothermal method was used to grow secondary $Bi_2Ti_2O_7$ nanostructures on TiO_2 submicron fibers. Electrospun TiO_2 submicron fibers were employed because the fiber matrix possesses the favorable morphology of high surface areas and aspect ratios [23, 24]. Moreover, it can serve as both reactant and substrate, ensuring close contact between $Bi_2Ti_2O_7$ nanostructures and TiO_2 submicron fibers for uniform growth of a hierarchical configuration. The hydrothermal process was performed in an alkaline environment where an aqueous solution of $Bi(NO_3)_3$ and submicron TiO_2 fibers were used as reactants [25–27]. The characterization results indicated that $Bi_2Ti_2O_7$ nanosheets with high crystallinity grew successfully on TiO_2 submicron fibers and well-defined three-dimensional hierarchical heterostructures of $Bi_2Ti_2O_7/TiO_2$ submicron fibers were formed. In contrast to pure TiO_2 and $Bi_2Ti_2O_7$, the composites showed significantly improved light absorption at a wavelength above 420 nm, as well as higher photocurrent density under a visible-light pulse. Photocatalytic tests revealed that the $Bi_2Ti_2O_7/TiO_2$ heterostructures have higher visible-light activity for degrading RhB than the pure $Bi_2Ti_2O_7$, and unmodified TiO_2.

Methods

TiO_2 submicron fibers were fabricated using the well-known process reported previously in Refs. [20, 23]. In the following hydrothermal procedure, 5 mg of the electrospun TiO_2 submicron fibers were placed into an autoclave containing two different $Bi(NO_3)_3$ solutions. The concentration of the $Bi(NO_3)_3$ solutions was 0.0103 and 0.0412 mmol L^{-1}, respectively. The pH value of the solution was adjusted to 13 using a 1 M KOH solution. The reaction was carried out at 180 °C for 24 h. The fabricated products were collected, washed with deionized water, and then dried in an oven at 60 °C for 6 h. Using this method, two different $Bi_2Ti_2O_7/TiO_2$ composites were produced, which were denoted as BT1 and BT2, respectively.

The structure and morphology of the prepared samples was investigated using powder X-ray diffraction (XRD; Bruker D8 Advance, using Cu*K*α radiation), scanning electron microscopy (SEM; Hitachi S-4800), and transmission electron microscopy (TEM; JEOL 2100). The optical properties of the samples were analyzed via UV-visible diffuse reflectance spectroscopy, recorded on a UV/Vis spectrophotometer (Shimadzu UV-2550) at room temperature. Photoelectrochemical measurements of the prepared samples were recorded with a laboratory-built electrochemical analyzer (CHI660E, China) consisting of a standard three-electrode system [20]. The $Bi_2Ti_2O_7/TiO_2$ heterojunction composite films served as working electrodes after coating the produced samples on $Au/SiO_2/Si$ substrates (10 × 10 mm). A 300-W Xe lamp, equipped with a 420 nm cutoff filter was used for excitation source.

To measure photocatalytic activity, a 100 ml of rhodamine B (RhB; 1.0×10^{-5}mol L^{-1}) solution with an initial concentration of 10 mg L^{-1} in the presence of solid catalyst was filled into a laboratory-built photoreactor. The photoreactor was equipped with an internal light source (150-W Xe lamp and a cutoff filter transmitting >420 nm) surrounded by a water-cooled quartz barrier to cool the lamp. The solution with the photocatalysts was stirred in the dark for 30 min to obtain a good dispersion and establish an adsorption-desorption equilibrium between the organic molecules and the catalyst surface. Changes in concentration of the dye solution were measured with a spectrophotometer at lambda of 553 nm at specified reaction intervals.

Results and Discussion

The crystal structures of $Bi_2Ti_2O_7/TiO_2$ composites were identified via XRD analysis, as shown in Fig. 1. The strong, sharp peaks indicated that the as-obtained products are highly crystallized. For the sample BT1, diffraction peaks at about $2\theta = 25.1°$, 37.4°, 48.2°, 54.1°, and 55.0° could be indexed perfectly to the (101), (004),

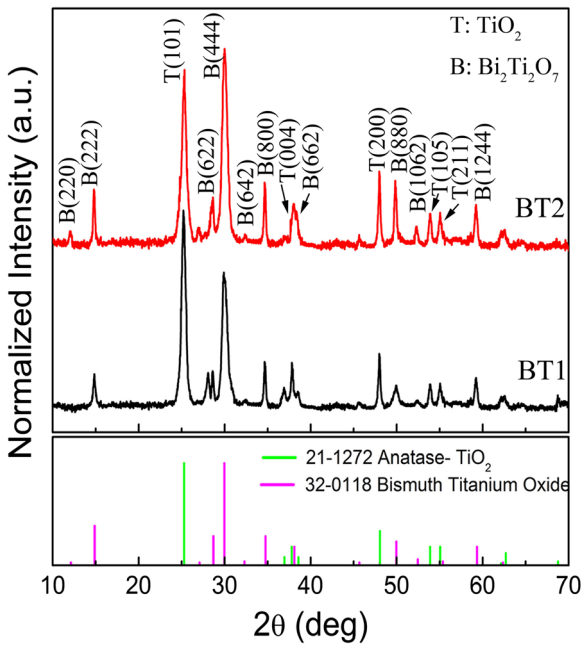

Fig. 1 XRD patterns of typical $Bi_2Ti_2O_7/TiO_2$ composites

(200), (105), and (211) crystal planes of anatase TiO_2 (JCPDS 21-1272,), respectively. Additional diffraction peaks appear with 2θ values of 14.9°, 28.8°, 30.2°, 32.1°, 34.6°, 37.8°, 49.6°, and 52.3°, which correspond to (222), (622), (444), (642), (800), (662), (880), and (10, 6, 2) crystal planes of the cubic phase of $Bi_2Ti_2O_7$, respectively (JCPDS 32-0118,). This suggests that part of TiO_2 has been successfully converted to $Bi_2Ti_2O_7$. For the sample BT2, the relative intensity of diffraction peaks for the ratio of BT2 to TiO_2 became stronger than that of BT1 to TiO_2. This suggests a higher yield of $Bi_2Ti_2O_7$ in sample BT2, which was further confirmed after observation with the SEM. Additionally, no impurity-attributed peaks were detected in the patterns of the XRD analysis. The XRD peaks of TiO_2 in the two $Bi_2Ti_2O_7/TiO_2$ composites did not shift compared with the standard diffractive peaks of pure anatase TiO_2, which indicates that Bi did not substitute Ti and enter the TiO_2 lattices. Therefore, it appears that the synthesis route was favorable for obtaining a multicomponent oxide composite that integrates the anatase phase of TiO_2 with $Bi_2Ti_2O_7$.

Figure 2 shows the morphologies and distribution of the mean diameters of the fibered samples. Before hydrothermal treatment, the TiO_2 submicron fibers with diameters about 200–600 nm had a relatively smooth surface without secondary nanostructures, and the average diameter was estimated to be about 380 nm, as shown in Fig. 2a, b. After the hydrothermal treatment, the samples remained as a non-woven fibrous morphology. However, the surface was no longer relatively smooth. Instead, the submicron fibers were decorated with numerous secondary nanosheets, as shown in Fig. 2c, d. After increasing the concentration of the $Bi(NO_3)_3$ precursor by a factor four, the density of the nanosheets grown on the surface of submicron fibers

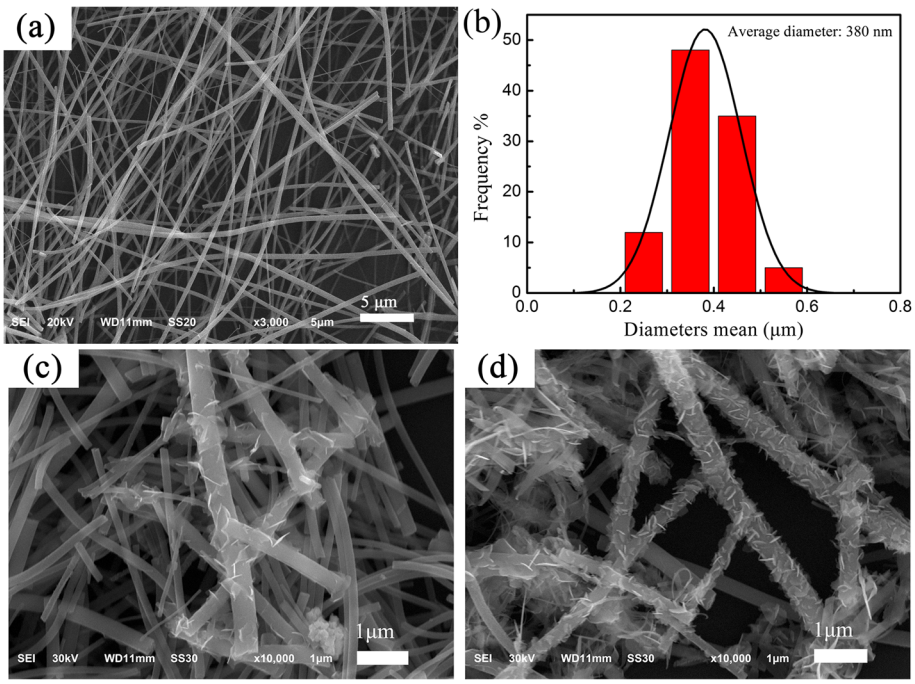

Fig. 2 **a** SEM images of TiO_2 submicron fibers and **b** the corresponding histogram of diameters distribution. **c**, **d** SEM images of the composition BT1 and BT2, respectively

increased significantly. This result is confirmed by the XRD analysis. The size of the nanosheets, however, showed no obvious changes. The nanosheets were still uniformly distributed along each fiber—without aggregation—although their density increased significantly. This might be because the high porosity and large surface area of the TiO_2 fibers favor both growth and uniform distribution of secondary nanostructures.

The typical TEM images of an individual hierarchical submicron fiber of sample BT2 were shown in Fig. 3. The $Bi_2Ti_2O_7$ that grew around the TiO_2 matrix shows a nanosheet configuration with a narrow and uniform size distribution, which is consistent with the SEM images in Fig. 3. The HRTEM image of the junction clearly showed two types of lattice fringes, as shown in Fig. 3b. For one set of fringes, the spacing is 0.35 nm, which corresponds to the (101) plane of the anatase crystal structure of TiO_2. For the other set of fringes, the spacing is 0.592 nm, which corresponds to the (111) lattice spacing of cubic $Bi_2Ti_2O_7$. The results suggest the presence of heterojunctions, which can improve both charge separation and charge transfer within the hybrid structure over pure $Bi_2Ti_2O_7$ and TiO_2. A selected area electron diffraction (SAED) pattern was characterized from a single nanosheet (Fig. 3c). The bright diffraction spots clearly reveal the high crystallinity of a single crystal $Bi_2Ti_2O_7$ nanosheet. Figure 3d shows elemental line mapping of Bi, Ti, and O concentrations along a radial direction of the $Bi_2Ti_2O_7/TiO_2$ composite fibers. All elements (Bi, Ti, and O) were observed to be

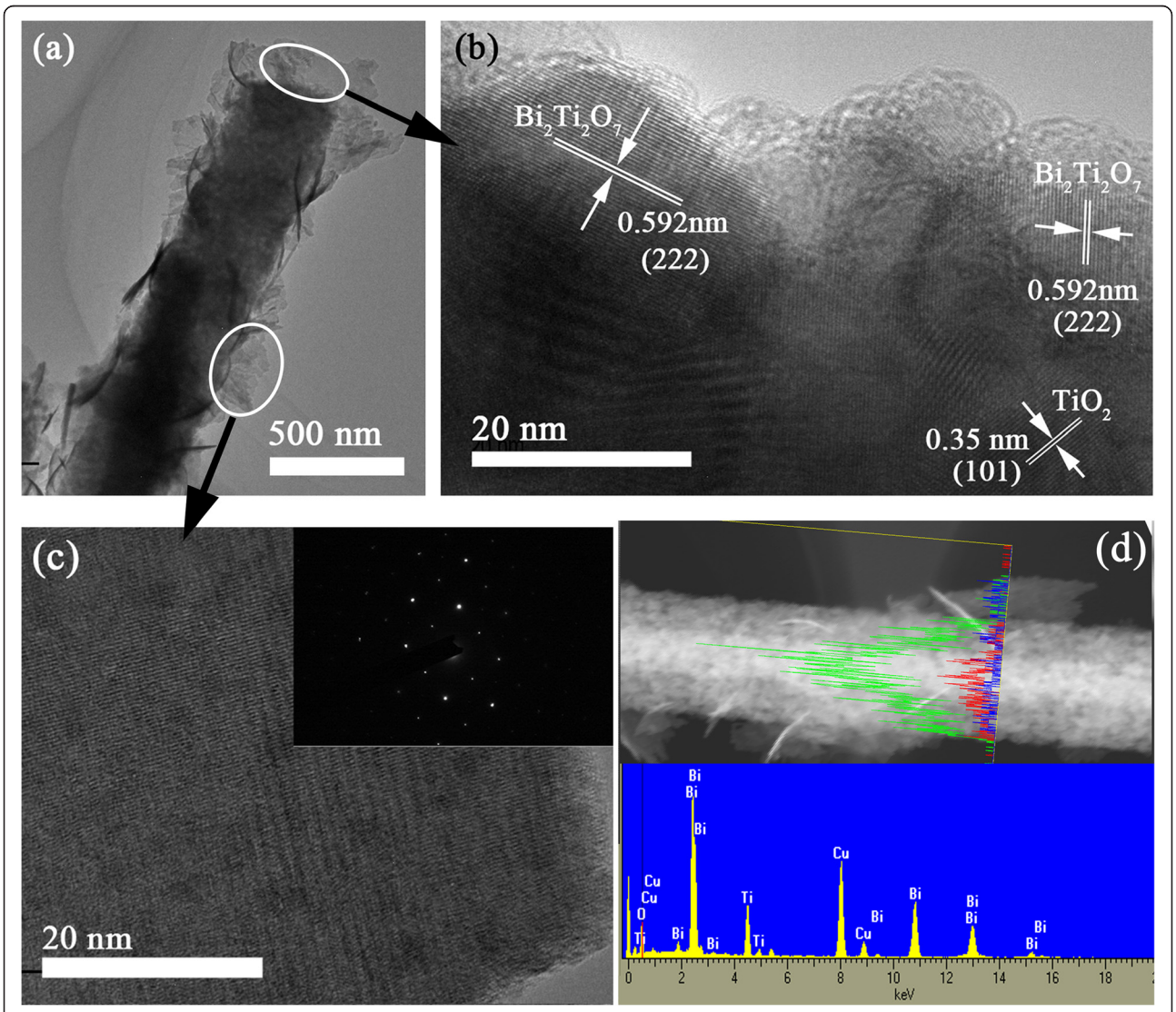

Fig. 3 **a** TEM image of $Bi_2Ti_2O_7/TiO_2$ composite fiber. **b** HRTEM image of heterojunction region. **c** HRTEM image of the nanosheet surface. The *inset* shows SAED of the single nanosheet. **d** Elemental line mapping along a radial direction of the $Bi_2Ti_2O_7/TiO_2$ fiber showing Bi (blue), Ti (red), and O (green) and EDX spectrum

homogeneously distributed in the fibers. Further, the quantitative analysis of the products was measured by using X-ray fluorescence (XRF) spectrum. As shown in Additional file 1: Figure S1, the molar ratio of $Bi_2Ti_2O_7$ to TiO_2 could be determined as 1/14 for BT1 and 1/3.5 for BT2, respectively. (Detailed derivation process is described in the supporting information.)

Figure 4 shows the UV-Vis absorption spectra of the composites BT1 and BT2, as well as pure phase TiO_2 submicron fibers and the $Bi_2Ti_2O_7$ hydrothermal product, which were converted from the corresponding diffusion reflectance spectra using the Kubelka-Munk function [27]. Pure anatase TiO_2 submicron fibers only showed fundamental absorption in the UV-light region, while $Bi_2Ti_2O_7$ displayed a portion of absorption in visible-light region. For the heterostructures, the curves of samples BT1 and BT2 showed a shift of the absorption edge toward longer wavelengths, i.e., into the visible-light region. The absorption of visible light showed a progressive red shift with the increasing density of the $Bi_2Ti_2O_7$ nanosheets grew on TiO_2 submicron fibers. This suggests a potential ability for photocatalytic decomposition of organic contaminants under irradiation with visible light. For semiconductors of the direct transition type, the relation curves of $(\alpha h\nu)^2$ versus band gap energy E_g were obtained using the equation (where α is absorption coefficient) [28, 29]: $h\nu - E_g = (\alpha h\nu)^2$. Therefore, their respective band gaps were calculated as 3.2, 2.94, 2.86, and 2.78 eV for pure TiO_2, $Bi_2Ti_2O_7$ and the heterostructured composites BT1 and BT2. The reduced band gap energy for heterostructures can be attributed to the formation of an internal electric field between $Bi_2Ti_2O_7$ and TiO_2, which causes the Fermi levels of the two materials to move toward each other and eventually reach the same potential. The improved light absorption of the composites creates more electron-hole pairs for unchanged visible-light irradiation, which subsequently results the potential of enhanced photocatalytic activity.

The photocatalytic degradation of RhB had been chosen as a model reaction to evaluate the photocatalytic activity of the present $Bi_2Ti_2O_7/TiO_2$ heterostructure. Adsorption in the dark was performed to ensure sufficient dispersion and an adsorption-desorption equilibrium between the organic molecules and the catalyst surface. Figure. 5a shows a series of plots of the RhB degradation efficiency (C/C_0) of four different photocatalysts: pure phase TiO_2 submicron fibers, $Bi_2Ti_2O_7$ hydrothermal product, and $Bi_2Ti_2O_7/TiO_2$ heterostructure submicron fibers (BT1 and BT2). The performance of RhB degradation without any catalyst also was carried out to be a comparison. C_0 and C represent the RhB concentration at reaction time 0 and t, respectively. The order of photocatalytic activities under visible-light irradiation was manifested as: BT2 > BT1 > $Bi_2Ti_2O_7$ > TiO_2. Furthermore, the kinetic linear simulation curves of RhB photocatalytic degradation for the four different photocatalysts were shown in Fig. 5b. The degradation of RhB by composites under visible-light irradiation is

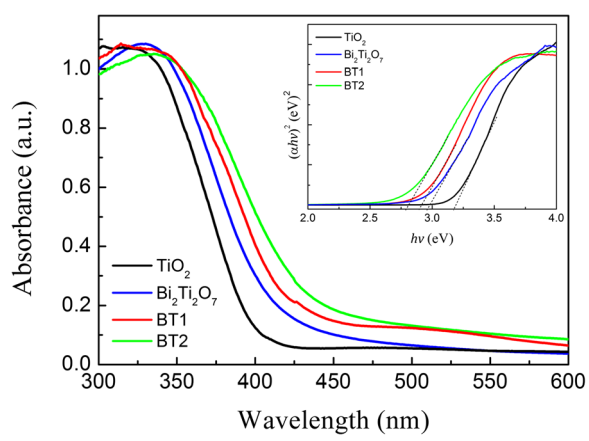

Fig. 4 UV-visible absorption spectra and (*inset*) the relationship between $(ahv)^2$ and band gap energy (E_g) for different samples

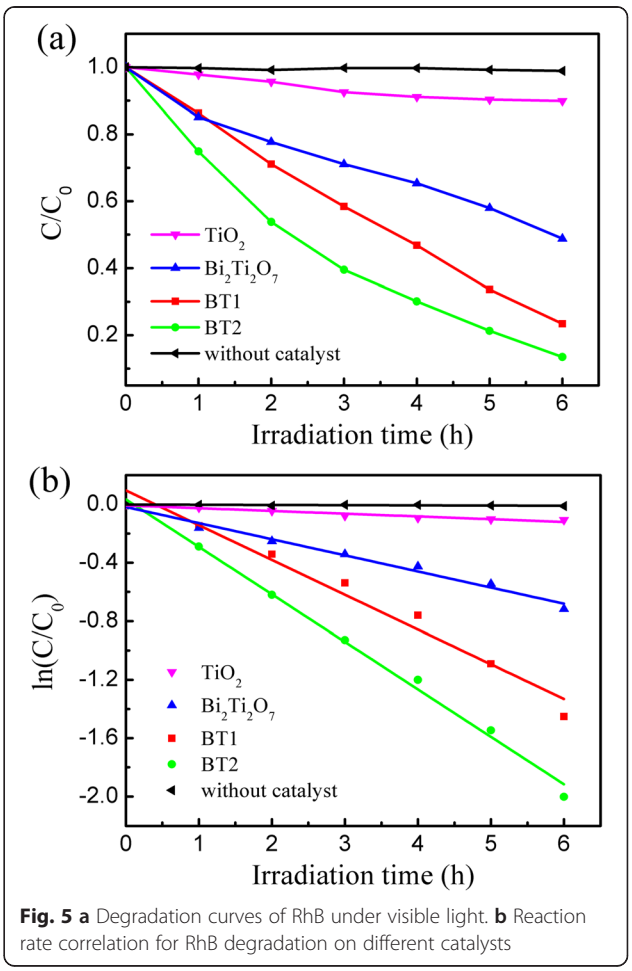

Fig. 5 a Degradation curves of RhB under visible light. **b** Reaction rate correlation for RhB degradation on different catalysts

known to follow the first-order Langmuire-Hinshelwood rate equation: $C = C_0 \cdot e^{-kt}$, where k (min^{-1}) denotes the pseudo-first-order rate constant of the reaction [8]. The rate constants (k) were calculated to be 3.13×10^{-4} min^{-1} for TiO_2 and 1.84×10^{-3} min^{-1} for $Bi_2Ti_2O_7$, as well as 3.97×10^{-3} min^{-1} for BT1 and 5.42×10^{-3} for BT2, respectively. For comparison, the photocatalytic performances of samples with different concentrations were shown in Additional file 1: Figure S2. The enhanced photocatalytic performance of the $Bi_2Ti_2O_7/TiO_2$ composite fibers was attributed to a synergistic effect between $Bi_2Ti_2O_7$ and TiO_2. Firstly, according to UV-Vis absorption analysis, the absorption edges of samples containing $Bi_2Ti_2O_7$ shifted toward longer wavelengths and into the visible-light region, which increases the production of electron-hole pairs under the same visible-light irradiation. Secondly, compared with single $Bi_2Ti_2O_7$ or TiO_2, the presence of nanoscale heterojunctions in the composites promoted charge separation but also suppressed the recombination of already photogenerated electron-hole pairs [18, 30]. This is further confirmed by photoelectrochemical measurements mentioned below.

The semiconducting nature of the $Bi_2Ti_2O_7/TiO_2$ composite fibers makes them suitable for the development of photoelectrochemical cells [28, 31]. In order to evaluate their relevant properties and further illustrate the enhanced electron transfer in the composites, the photocurrent – time ($I - t$) curves with several on-off cycles of intermittent visible-light irradiation were carried out, as shown in Fig. 6. The photocurrent responded immediately and rapidly increased to reach and maintain a constant value immediately after irradiation started. The photocurrent rapidly decreased and reached zero when the illumination stopped. This effect was reproduced and confirmed many times. The $Bi_2Ti_2O_7/TiO_2$ composite electrodes showed a strong instant photoresponse upon illumination with visible light, and provided a stable photocurrent values (0.72 μA cm^{-2} for BT1, and 1.44 μA cm^{-2} for BT2), which is considered to be superior to the TiO_2 electrode (0.4 μA cm^{-2}). The magnitude of the photocurrent is a measure of charge collection efficiency at the electrode surface. More electron-hole pairs were produced in BT2 with the greater density in hierarchical $Bi_2Ti_2O_7$ compared to BT1, which results a higher photocurrent under the same visible-light irradiation. Moreover, the photoelectrochemical responses are identical, which confirms that the higher photocurrent solely originates from the coupling between $Bi_2Ti_2O_7$ and TiO_2.

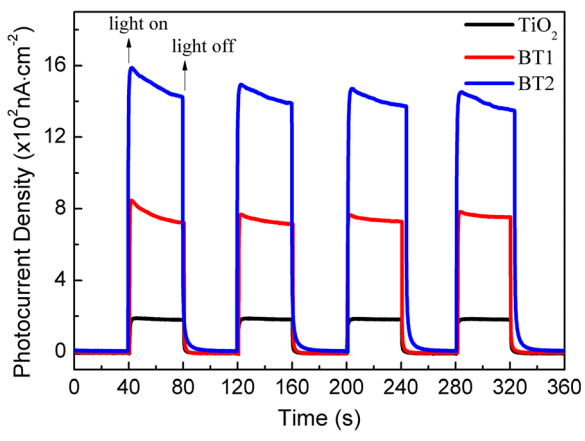

Fig. 6 Photocurrent density versus time plotted for the different samples

It is evident that the enhanced activity of the hybrid photocatalyst involving $Bi_2Ti_2O_7$ and TiO_2 can be attributed to the synergistic effects between visible light sensitization and the presence of heterojunctions. The CB and VB positions of semiconductor could be calculated using the empirical equation: $E_{CB} = X - E_e - 0.5E_g$, where X is the geometric mean of Mulliken's electron negativities of constituent atoms, E_e is the energy of free electrons on the hydrogen scale (about 4.5 eV), and E_g is the band gap energy [26]. When $Bi_2Ti_2O_7$ is in contact with TiO_2 to form a heterojunction, the Fermi levels of $Bi_2Ti_2O_7$ and TiO_2 tend to descend and ascend, respectively. This indicates that an inner electric field is created at the interface, followed by the formation of an equilibrium. It is known that photocatalytic processes are based on electron-hole pairs generated by means of band gap excitation. The generation and separation of the electron-hole pairs are the key factors to influence a photocatalytic reaction [30]. In this case, the RhB degradation over the $Bi_2Ti_2O_7/TiO_2$ composite under visible-light irradiation was carried out through several pathways, as illustrated in Fig. 7. The photogenerated electron-hole pairs were produced in $Bi_2Ti_2O_7$ nanosheets after being excited with visible light with energies below 2.94 eV ($\lambda > 420$ nm). The generated electrons in the $Bi_2Ti_2O_7$ nanosheets then migrated to the CB of TiO_2, leaving holes in the VB of $Bi_2Ti_2O_7$. As a result, the higher charge separation rate increased the lifetime of the charge carriers and enhanced the efficiency of the interfacial charges transferred to the adsorbed substrates, which in turn leads to higher activity of the $Bi_2Ti_2O_7/TiO_2$ composite photocatalyst. Meanwhile, the electrons (e^-) generated in the CB react with dissolved oxygen molecules to produce superoxide radical anions $\cdot O_2^-$. The latter generates, via protonation, the hydroperoxy radicals $\cdot HO_2$, which produce the hydroxyl radicals ·OH. The ·OH is a strong oxidizing agent to decompose the organic dye. The effect of reactive oxygen species (··OH and $\cdot O_2^-$) on the degradation of RhB was investigated by introducing isopropanol (IPA) and ammonium oxalate (AO) as the scavengers of ·OH and O_2^-, respectively. The

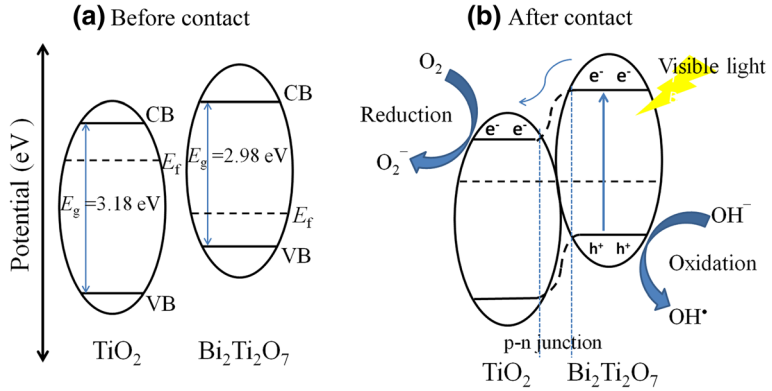

Fig. 7 Schematic diagram of **a** the band energy of $Bi_2Ti_2O_7$ and TiO_2 before contact; **b** the formation of a p-n junction and the process of electron-hole pairs separation and transfer under visible-light irradiation

quenching of the reaction containing scavengers indicated that ·OH is significant reactive species in the TiO_2-catalyzed photocatalytic oxidation process [31, 32] (see Additional file 1: Figure S3 for photocatalytic performances of RhB aqueous solution containing scavengers). The reactions related to the degradation of RhB could be referred to the relevant literatures elsewhere [8, 18, 19, 31–34].

Conclusions

In summary, a composite photocatalyst of $Bi_2Ti_2O_7/TiO_2$ heterostructured submicron fibers was synthesized via an in situ hydrothermal method. SEM and TEM observation revealed that the as-synthesized sample is micro-sized fiber-like hierarchy configuration consisted of $Bi_2Ti_2O_7$ nanosheets decorated with the primary TiO_2 submicron fibers. Extension of the light absorption from the ultraviolet region to the visible-light region was confirmed by UV-vis absorption spectra. The heterostructure of the $Bi_2Ti_2O_7/TiO_2$ composite exhibited enhanced visible photocatalytic activity over that of the pure $Bi_2Ti_2O_7$ and TiO_2 in the decomposition of RhB in water. The enhanced photocatalytic activity can be attributed to the extended absorption in the visible-light region and the effective separation of photogenerated carriers driven by the inner potential generated at the $Bi_2Ti_2O_7/TiO_2$ junction interface, which was demonstrated by the measurement of photocurrent response. Moreover, such a simple and versatile method could enable the use of TiO_2 submicron fibers as precursor materials and templates to fabricate many other ternary titanate-based heterostructures for environmental applications and solar cell devices [35, 36].

Additional file

Additional file 1: Figure S1. (a) and (b) The morphology images of the composition BT1 and BT2, respectively; (c) The XRF quantitative analysis of the molar ratio of $Bi_2Ti_2O_7/TiO_2$ in the corresponding composition BT1 and BT2. **Figure S2.** (a) Degradation curves and (b) reaction rate correlation of solid catalysts with different concentration in RhB aqueous solution. **Figure S3.** The effects of active species (·OH and $\cdot O_2^-$) on the degradation of RhB during the photocatalytic process. Detail derivation process for the molar ratio of $Bi_2Ti_2O_7$ to TiO_2. (DOC 2.82 mb)

Abbreviations

BT1: $Bi_2Ti_2O_7/TiO_2$ composites with molar ratio of 1/14; BT2: $Bi_2Ti_2O_7/TiO_2$ composites with molar ratio of 1/3.5; CB: conduction band; JCPDS: Joint Committee on Powder Diffraction Standards; RhB: rhodamine B; SEM: scanning electron microscopy; TEM: transmission electron microscopy; UV: ultraviolet; UV-vis: UV-visible; VB: valence band; XRD: X-ray diffraction.

Competing Interests

The authors declare that they have no competing interests.

Authors' Contributions

DZ designed the experiment and drafted the manuscript. HY and ZH completed the synthesis of $Bi_2Ti_2O_7/TiO_2$ submicron fibers composites. YFT, YT, and YC carried out the series characterization of the samples and interpreted the data. XZ participated in revised this manuscript. All authors read and approved the final manuscript.

Acknowledgements

The authors thank the generous financial support from the National Science Foundation of China (NSFC, Grant No. 51502114, 61405076 and 11304124), Natural Science Foundation of Hubei Province in China (Grant No. 2013CFB38), and Natural Science Foundation of Hubei Provincial Department of Education (Grant No. Q20141005 and Q20142805). The authors would like to extend their sincere appreciation to the Collaborative Innovation Center of Hubei University for XRD, SEM, and TEM measurements.

Author details

[1]School of Physics and Information Engineering, Jianghan University, Wuhan 430056, China. [2]Faculty of Physics and Electronic Technology, Hubei University, Wuhan 430062, China. [3]Laboratory of Low-Dimension Functional Nanostructures and Devices, Hubei University of Science and Technology, Xianning 437100, China.

Received: 6 February 2016 Accepted: 4 April 2016
Published online: 12 April 2016

References

1. Chen X, Shen S, Guo L, Mao S (2010) Semiconductor-based photocatalytic hydrogen generation. Chem Rev 110:6503–6570
2. Lin J, Liu XL, Zhu S, Liu YS, Chen XF (2015) Anatase TiO_2 nanotube powder film with high crystallinity for enhanced photocatalytic performance. Nanoscale Res Lett 10:110

3. Wong TS, Kang SH, Tang SK, Smythe EJ, Hatton BD, Grinthal A, Aizenberg J (2011) Bioinspired self-repairing slippery surfaces with pressure-stable omniphobicity. Nature 477:443–447
4. Kumar SG, Devi LG (2011) Review on modified TiO_2 photocatalysis under UV/Visible light: selected results and related mechanisms on interfacial charge carrier transfer dynamics. J Phys Chem A 115(46):13211–13241
5. Cao TP, Li YJ, Wang CH, Shao CL, Liu YC (2011) A facile in situ hydrothermal method to $SrTiO_3/TiO_2$ nanofiber heterostructures with high photocatalytic activity. Langmuir 27(6):2946–2952
6. Tokarcikova M, Tokarsky J, Cabanova K, Matejka V, Mamulova KK, Seidlerova J (2014) The stability of photoactive kaolinite/TiO_2 composite. Compos Part B: Eng 67:262–269
7. Zhu J, Cao Y, Bian Z, Wang S, Hou Y, Li H, Lu Y (2012) Synthesis of photocatalytic TiO_2 with controlled hierarchical structure by alcohol-induced assembly. Sci Sin Chim 42(11):1627–1635
8. Alessandro DM, Massimo Z, Mario S, Giuseppe N, Maria EF, Giuliana I (2015) Effect of P_t nanoparticles on the photocatalytic activity of ZnO nanofibers. Nanoscale Res Lett 10:484
9. Zhou D, Zhou YH, Tian Y, Tu YF, Zheng G, Gu HS (2015) Structure and piezoelectric properties of lead-free $Na_{0.5}Bi_{0.5}TiO_3$ nanofibers synthesized by electrospinning. J Mater Sci & Technol 31:1181–1185
10. Ivicheva SN, Kargin YF, Kutsev SV, Ashmarin AA (2015) Synthesis of different bismuth titanates and ordered Bi-Ti-O nanocomposites based on opal matrices. Russ J Inorg Chem 60(11):1317–1328
11. Kargin YF, Ivicheva SN, Volkov VV (2015) Phase relations in the Bi_2O_3-TiO_2 system. Russ J Inorg Chem 60(5):619–625
12. Zhao WW, Zhang CY, Liu YW, Huang XP, Mao F (2011) Visible-light photocatalytic activity of the $Bi_2Ti_4O_{11}$ nanorods. Adv Mater Res 306–307: 1416–1419
13. Pei LZ, Liu HD, Lin N, Yu HY (2015) Bismuth titanate nanorods and their visible light photocatalytic properties. J Alloy Compd 622:254–261
14. Zhou TF, Hu JC (2010) Mass production and photocatalytic activity of highly crystalline metastable single-phase $Bi_{20}TiO_{32}$ nanosheets. Environ Sci Technol 44(22):8698–8703
15. Ni F, Luo LH, Pan XY, Li WP, Zhu JQ (2012) Effects of A-site vacancy on the electrical properties in lead-free non-stoichiometric ceramics $Bi_{0.5+x}(Na_{0.82}K_{0.18})_{0.5-3x}TiO_3$ and $Bi_{0.5+y}(Na_{0.82}K_{0.18})_{0.5}TiO_3$. J Alloy Compd 541: 150–156
16. Bian ZF, Huo YN, Zhang Y, Zhu J, Lu YF, Li HX (2009) Aerosol-spay assisted assembly of $Bi_2Ti_2O_7$ crystals in uniform porous microspheres with enhanced photocatalytic activity. Appl Catal B Environ 91:247–253
17. Ren JK, Liu GQ, Wang YP, Shi Q (2012) A novel method for the reparation of $Bi_2Ti_2O_7$ pyrochlore. Mater Lett 76:184–186
18. Zhang ZY, Jiang CY, Du P, Wang YP (2015) Synthesis and characterization of $Bi_2Ti_2O_7/TiO_2$ heterojunction by glycerol-assisted alcoholthermal method. Ceram Int 41:3932–3939
19. Hou J, Qu Y, Krsmanovic D, Ducati C, Eder D, Kumar R (2010) Hierarchinal synthesis of bismuth titanate complex architectures and their visible-light photocatalytic activities. J Mater Chem 20:2418–2423
20. Liu H, Chen YJ, Tian GH, Ren ZY, Tian CG, Fu HG (2015) Visible-light-induced self-cleaning property of Bi2Ti2O7-TiO2 composite nanowire arrays. Langmuir 31:5962–5969
21. Hu ML, Fang MH, Tang C, Yang T, Huang ZH, Liu YG, Wu XW, Min X (2013) The effects of atmosphere and calcined temperature on photocatalytic activity of TiO_2 nanofibers prepared by electrospinning. Nanoscale Res Lett 8:548
22. Jiang Z, Tijing LD, Amarjargal A, Park CH, An KJ, Shon HK, Kim CS (2015) Removal of oil from water using magnetic bicomponent composite nanofibers fabricated by electrospinning. Compos Part B: Eng 77:311–318
23. Nasser AM, Mohammad AA, Mohamed EN, Hak YK (2013) Influence of the nanofibrous morphology on the catalytic activity of NiO nanostructures: an effective impact toward methanol electrooxidation. Nanoscale Res Lett 8:402
24. Zhao JG, Jia CW, Duan HG, Li H, Xie EQ (2008) Structural properties and photoluminescence of TiO_2 nanofibers were fabricated by electrospinning. J Alloy Compd 461(1-2):447–450
25. Tsai CJ, Yang CY, Liao YC, Chueh YL (2012) Hydrothermally grown bismuth ferrites: controllable phases and morphologies in a mixed KOH/NaOH mineralizer. J Mater Chem 22:17432–17436
26. Cao TP, Li YJ, Wang CH, Zhang ZY, Zhang MY, Shao CL, Liu YC (2011) $Bi_4Ti_3O_{12}$ nanosheets/TiO_2 submicron fibers heterostructures: in situ fabrication and high visible light photocatalytic activity. J Mater Chem 21:6922–6927
27. Zhang J, Huang LH, Liu PL, Wang Y, Jiang XD, Zhang EP, Wang HB, Kong Z, Xi JH, Ji ZG (2016) Heterostructure of epitaxial (001) $Bi_4Ti_3O_{12}$ growth on (001) TiO_2 for enhancing photocatalytic activity. J Alloy Compd 654:71–78
28. Ren K, Gan YX, Young TJ, Moutassem ZM, Zhang LH (2013) Photoelectrochemical responses of doped and coated titanium dioxide composite nanotube anodes. Compos Part B: Eng 52:292–302
29. Hou DF, Hu XL, Hu P, Zhang W, Zhang MF, Huang YH (2013) $Bi_4Ti_3O_{12}$ nanofibers-BiOI nanosheets p-n junction: facile synthesis and enhanced visible-light photocatalytic activity. Nanoscale 5:9764–9772
30. Fan HM, Li HY, Liu BK, Lu YC, Xie TF, Wang DJ (2012) Photoinduced charge transfer properties and photocatalytic activity in $Bi_2O_3/BaTiO_3$ composite photocatalyst. ACS Appl Mater Interfaces 4(9):4853–4857
31. Peng C, Yang XF, Li YH, Yu H, Wang HJ, Peng F (2016) Hybrids of two-dimensional Ti_3C_2 and TiO_2 exposing {001} facets toward enhanced photocatalytic activity. ACS Appl Mater Interfaces 8:6051–6060
32. Xian T, Yang H, Di LJ, Ma JY, Zhang HM, Dai JF (2014) Photocatalytic reduction synthesis of $SrTiO_3$-graphene nanocomposites and their enhanced photocatalytic activity. Nanoscale Res Lett 9:327
33. Zhang J, Bang JH, Tang C, Kamat PV (2010) Tailored TiO_2-$SrTiO_3$ heterostructure nanotube arrays for improved photoelectrochemical performance. ACS Nano 4(1):387–395
34. Gupta S, Subramanian VR (2014) Encapsulating $Bi_2Ti_2O_7$ (BTO) with reduced graphene oxide (RGO): an effective strategy to enhance photocatalytic and photoelectrocatalytic activity of BTO. ACS Appl Mater Interfaces 6:18597–18608
35. McLeod JA, Green RJ, Kurmaev EZ, Kumada N, Belik AA, Moewes A (2012) Band-gap engineering in TiO_2-based ternary oxides. Phys Rev B 85:195201
36. Sabba D, Agarwala S, Pramana SS, Mhaisalkar S (2014) A maskless synthesis of TiO_2-nanofiber-based hierarchical structures for solid-state dye-sensitized solar cells with improved performance. Nanoscale Res Lett 9:14